THE JOURNAL OF PHYSICAL CHEMISTRY C
A JOURNAL OF THE AMERICAN CHEMICAL SOCIETY

pubs.acs.org/JPCC

Article

Tunable Dielectric Properties of Nickel Ferrite Derived via Crystallographic Site Preferential Cation Substitution

Pendaranahalli Nadikeraiah Anantharamaiah,* Prerna Rao, Hadonahalli Munegowda Shashanka, Vijay Khopkar, Jeyaramane Arout Chelvane, Balaram Sahoo, and C. V. Ramana*

Cite This: *J. Phys. Chem. C* 2022, 126, 9123−9134

Read Online

ACCESS | Metrics & More | Article Recommendations

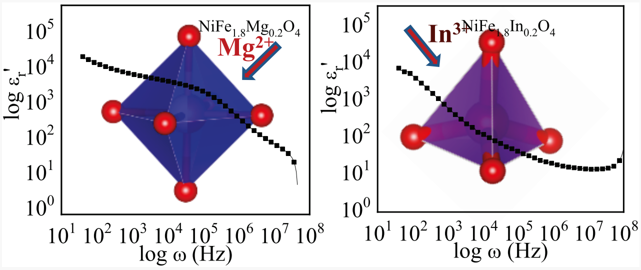

ABSTRACT: We report on the tunable dielectric properties achieved in cation-substituted nickel ferrite ($NiFe_2O_4$; NFO) by selectively engineering the crystallographic site occupation of the dopant cation in the NFO ceramics. The NFO, Mg-substituted NFO ($NiMg_{0.2}Fe_{1.8}O_4$; NMFO), and In-substituted NFO ($NiIn_{0.2}Fe_{1.8}O_4$; NIFO) nanocrystals were synthesized by employing a tartrate-gel chemical route, followed by calcination at 500 °C. High-resolution transmission electron microscopy (HRTEM) analyses indicate the crystal quality of NFO, NMFO, and NIFO nanomaterials. The HRTEM data revealed that all of the ferrite materials were nanocrystalline with sizes in the range of 15−25 nm. Coupled with HRTEM analyses, X-ray diffraction analyses indicate the formation of single-phase spinel-structured NFO, NMFO, and NIFO materials without any detectable impurities. Chemical analysis performed using Mossbauer spectroscopy indicates that Mg^{2+} occupies the octahedral site, while In^{3+} preferably occupies the tetrahedral site of the spinel-structured NFO. The Fourier transform infrared (FTIR) absorption bands corresponding to metal−oxygen (M−O) intrinsic stretching vibration in the octahedral unit (MO_6) and the tetrahedral unit (MO_4), respectively, were noted in all of the samples. However, the trend in the frequency shift of these bands in Mg- and In-substituted NFO materials is different due to the occupation of different sites of Mg and In as confirmed by Mossbauer studies. The electronic structure and chemical valence state analysis using X-ray photoelectron spectroscopy (XPS) corroborates with chemical bonding analyses performed by FTIR and cation distribution evaluation carried out by Mossbauer spectroscopy. The energy-dispersive X-ray spectrometry (EDS) data, in addition to XPS and FTIR analyses, further validate the formation of uniform and chemically homogeneous samples. The corresponding cation distribution revealed from Mossbauer studies correlates with the variation of dielectric properties of the doped NFO samples with respect to intrinsic NFO. At room temperature, the dielectric constant (ε) of NFO and NMFO is found to be nearly the same and constant over a wide range of frequencies. However, in NIFO, ε decreases with the applied frequency. The differences are attributed to the size effect and site preference of dopants (Mg^{2+} and In^{3+}). Irrespective of the dopants, an increase in the temperature enhances the dielectric constant, which is due to an increase in the number of free charge carriers. A thermally activated electrical conduction mechanism was operative in NFO, NMFO, and NIFO materials. The activation energies for NFO, NFMO, and NIFO were 18.84, 34.48, and 57.14 meV, respectively. The enhanced dipolar effect of In^{3+} at the tetrahedral site compared to Mg^{2+} at the octahedral site may be the origin of the relatively higher value of activation energy in NIFO compared to intrinsic and Mg-substituted NFO.

INTRODUCTION

Nickel ferrite ($NiFe_2O_4$; NFO) is one of the metal-oxide-based soft magnetic materials owing to its high magnetization at low magnetic fields and low coercive force.[1,2] The physical, chemical, and electromagnetic properties of NFO and NFO-based composites are attractive for utilization in numerous scientific and technological applications.[3−10] Due to the intrinsic nature of NFO, it has been employed as a suitable active material in a wide range of applications, which include electronic memory, biomedical sensors and actuators, telecommunication, electromagnetic interference (EMI) shielding, catalysis, energy storage, and high-frequency electromagnetic devices.[3−10] The recent attention to the intrinsic and doped NFO materials is primarily due to the possibility of the design and development of their nanoscale architectures for utilization in electromagnetics, electrochemical energy storage and conversion technologies, and biomedical applications.[3−10]

Received: January 21, 2022
Revised: April 22, 2022
Published: May 23, 2022

https://doi.org/10.1021/acs.jpcc.2c00529
J. Phys. Chem. C 2022, 126, 9123−9134

Additionally, using intrinsic or doped NFO in multilayered structures or in conjunction with polymers has been proposed to design highly efficient EMI shielding materials.[3] For instance, the EMI absorber materials designed by means of a multilayer assembly of poly(vinylidene fluoride)-containing Zn-doped NFO have shown to increase the EMI shielding effectiveness dramatically.[3] The highest absorbance (>91%) was reported for a multilayer assembly with a tailored composition and layering sequence.[3] Therefore, understanding the electrical, magnetic, and dielectric properties of intrinsic and doped NFO nanomaterials warrants further investigations. Furthermore, compared to bulk materials, transition-metal-based engineered nanostructured materials are expected to provide excellent opportunities to tailor and/or manipulate the quantum effects and thereby derive novel electrical, optical, and magnetic properties.[5−15]

From the crystal structure point of view, NFO belongs to the cubic spinel ferrite category and crystallizes in the inverse spinel structure (Figure 1a).[11] Represented by the general chemical formula of AB_2O_4, all Ni^{2+} ions are situated in octahedral sites (B-sites) and equal amounts of Fe^{3+} ions are disseminated in tetrahedral sites (A-sites) and octahedral sites (Figure 1b,c) in the spinel structure.[11] Each NFO unit cell consists of eight tetrahedral sites occupied by Fe^{3+} and 16 octahedral sites occupied by equal amounts of divalent (Ni^{2+}) and trivalent (Fe^{3+}) metal ions, leading to a perfect inverse spinel structure (Figure 1). In practice, $NiFe_2O_4$ manifests a slightly mixed spinel structure due to the presence of a small fraction of Ni^{2+} in the A-site. The distribution of cations between the two distinguishable sublattices depends solely on the synthesis methods and processing conditions. When doped with other metal ions, the properties of the parent NFO change depending on the nature and site preferences of the dopant cations.

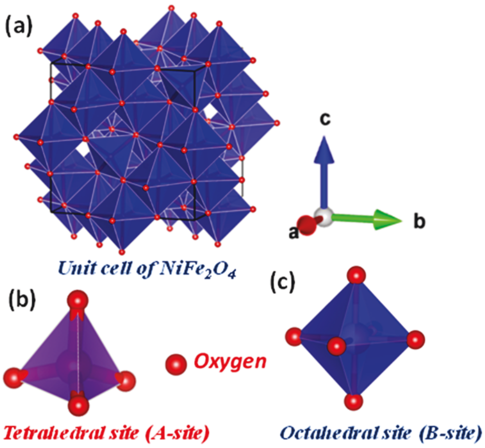

Figure 1. Crystal structure of a cubic spinel ferrite. (a) $NiFe_2O_4$ spinel ferrite structure with the representation of the unit cell, (b) tetrahedral (A) site, and (c) octahedral (B) site.

Nickel ferrite offers numerous ways to obtain desirable properties and/or tailor the structure and properties at the nanoscale dimensions, although researchers often aim at achieving tunable magnetic and electrical properties.[11−20] Apart from variable synthetic procedures, strategies, and processing conditions, metal-ion doping is one of the promising routes to achieve desirable properties in NFO.[11−14] Typically, the dopant ionic size must be comparable to the size of metal cation (Ni or Fe in NFO), resulting in the formation of a well-defined solid solution, without any secondary phases. In addition to the size of the dopant ion, the nature (magnetic or nonmagnetic), crystallographic site preference (A-site or B-site), amount of substitution (lower or higher), and ionic charge (chemical valence state) of the dopant ion are also crucial parameters in tuning the properties of the parent NFO compound. Therefore, the choice of metal ion for doping is the most important aspect to obtain the desired properties of NFO.

A wealth of information is available in the literature, where various dopant-induced effects on the structure and properties of nickel ferrites are evident.[15−23] Also, plenty of reports are available on the dielectric properties of nanocrystalline NFO and doped NFO.[15−18] However, based on the studies available in the literature and the aforementioned structural details, it is quite important to understand the effect of crystallographic site preference of the cations on the magnetic and electrical properties. Specifically, a comparative study of the metal cations with the same composition but different site preferences in NFO can provide clues to manipulate the properties and performance. Therefore, we focused our attention on the effect of Mg and In cations substituted in NFO with a fixed chemical composition to elucidate the effect of site occupancy of the cations on the magnetic and dielectric properties. Also, studies on the temperature-dependent dielectric properties of nickel ferrite and its derivatives (mainly In^{3+}- and Mg^{2+}-substituted NFO) are limited and yet to be explored thoroughly. Recently, we have investigated the synthesis, structure, and magnetostrictive properties of nickel ferrite and Mg^{2+}- and In^{3+}-doped nickel ferrite samples sintered from their nanocrystalline powders.[24] The present study focused on elucidating the effect of cation site preference on the dielectric properties of NFO and Mg- and In-doped NFO. To gain a deeper understanding and accurately determine such site preference-induced effects, we relied on estimating the cation distribution and deriving a correlation between the dielectric properties and chemical cation distribution in these ferrites. Mg^{2+} and In^{3+} ions are considered primarily due to differences in their size, charge, and crystallographic site preference. Interestingly, as presented and discussed in this paper, the crystallographic site preference of the dopant ion has a significant impact on the dielectric behavior of nickel ferrites.

■ MATERIALS AND METHODS

Synthesis. The intrinsic and Mg- and In-substituted Ni-ferrite ($NiFe_2O_4$, $NiFe_{1.8}Mg_{0.2}O_4$, and $NiFe_{1.8}In_{0.2}O_4$) nanomaterials were synthesized by a tartrate-gel method. We followed the previously established synthetic procedure to obtain the NFO, NMFO, and NIFO nanomaterials.[24] Briefly, a homogeneous solution of respective metal nitrates ($Fe(NO_3)_3\cdot 9H_2O$, $Ni(NO_3)_2\cdot 6H_2O$, and $Mg(NO_3)_2\cdot 6H_2O$) with high purity was mixed with 75 mL of tartaric acid (1.5 moles per metal ion). The metal nitrates were weighed according to stoichiometry. The chemical reaction mixture, thus prepared, was then subjected to continuous stirring for 30 min at 50 °C. For this metal tartrate solution, the polymerizing agent ethylene glycol (TA/EG with a ratio of 70:30) was added while increasing the reaction temperature to 75 °C. The solvent molecules expelled from the reaction mixture yielded a thick brownish viscous gel, which was then dried at 80 °C. Subsequently, the dried gel was ground to obtain a fine powder, which was calcined at 500 °C for 2 h. Characterization

https://doi.org/10.1021/acs.jpcc.2c00529
J. Phys. Chem. C 2022, 126, 9123−9134

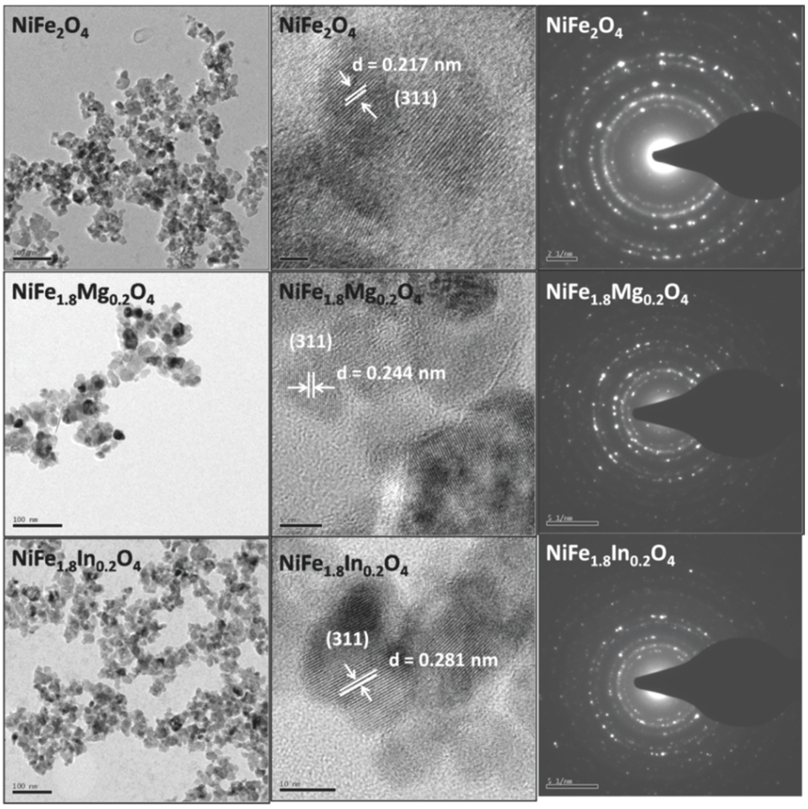

Figure 2. HRTEM data and selected area electron diffraction (SAED) patterns of NFO, NMFO, and NIFO nanoferrites. The left panel shows the TEM images of NFO, NMFO, and NIFO nanomaterials. The agglomeration and size variation (15−25 nm) of nanoferrites are evident. The middle panel shows the high-resolution TEM images of the samples. The crystalline nature of the samples is evident by the presence of lattice fringes. The values of lattice fringe spacing are as indicated in the images. The right panel shows the SAED patterns of the nanoferrites.

(discussed in the subsequent section) of the calcined powders thus obtained was carried out to confirm the phase purity of the calcined ferrite powders. After confirmation, these nanocrystalline powders were wetted with minimum amounts (2%) of a poly(vinyl alcohol) (PVA) solution and compacted into disk-shaped pellets. The green pellets were then sintered at 1200 °C for 2 h in a furnace atmosphere. The samples thus obtained were subjected to further characterization to probe the structural and dielectric properties.

Characterization. High-resolution transmission electron microscopy (HRTEM) (FEI Tecnai G2 F30 with an applied voltage of 300 kV) measurements were performed on the NFO, NMFO, and NIFO samples. The crystal structure, morphology, and microstructure of the ferrite samples were studied to understand the effect of Mg- and In- cation substitution. Additionally, X-ray diffraction (XRD) measurements were also made on these ferrite samples using a PANalytical X'pert pro diffractometer. The elemental analysis and chemical homogeneity of the samples were examined by means of energy-dispersive X-ray spectrometry (EDS) measurements. The EDS spectra of the samples were recorded using a scanning electron microscope (TESCAN VEGA3 LMU) equipped with an EDS detector. Fourier transform infrared (FTIR) spectroscopy was employed to understand the chemical bonding in the NFO, NMFO, and NIFO samples. The FTIR spectra of all of the samples were recorded at room temperature using an FTIR spectrometer (Bruker, Alpha-P, Diamond ATR cell). The electronic structure, chemical composition, and valence states of various cations were probed by means of X-ray photoelectron spectroscopy (XPS). The XPS spectra of the samples were recorded using a Thermo K-alpha+ spectrometer equipped with a monochromatic Al Kα X-ray source with an energy of 1486.6 eV. Mössbauer spectra were recorded with a constant-acceleration drive, driven in synchronization, having a 512-channel analyzer using a ^{57}Co radioactive source with 30 mCi activity. Calibration of the Mössbauer spectrometer was carried out using an enriched iron foil. The dielectric properties of the NFO, NMFO, and NIFO samples were recorded using an impedance analyzer (HP 4294A, Agilent technologies). The measurements were made in the temperature range of 25−200 °C and by varying the frequency (40 Hz−100 MHz).

■ RESULTS AND DISCUSSION

Crystal Structure, Phase, Microstructure, and Morphology. *Transmission Electron Microscopy (TEM).* The TEM images of NFO, NMFO, and NIFO are presented in Figure 2 (left panel). As revealed from these TEM images, the ferrite particles are nearly spherical in shape and agglomerated into clusters. This is the common feature that can be noted in all of the samples. The agglomeration into clusters occurs in these ferrite nanomaterials due to the magnetic nature of the nanoparticles. The average particle size of the samples is in the range of 15−25 nm.

The high-resolution TEM (HRTEM) images of the samples, shown in the middle panel of Figure 2, revealed the presence of lattice fringes, which signifies that the NFO, NMFO, and NIFO ferrites are crystalline in nature. The spacing between the crystal planes (*d*-spacing) of the samples was measured from the HRTEM images using digital micrograph software, and the values are given in the respective images. The *d*-spacing value determined for intrinsic NFO was 0.217 nm, which corresponds to the lattice spacing of the (311) planes. Interestingly, the analyses revealed that the *d*-spacing values increase in Mg- and In-substituted NFO. The corresponding *d*-spacing value for NMFO was 0.244 nm, while it was 0.281 nm for NFIO. The two general remarks derived from these observations are the following. The increased *d*-spacing values demonstrate that the dopants (Mg^{2+} and In^{3+}) successfully integrated into the spinel Ni-ferrite lattice framework. Thus, this first observation validates the synthesis process and processing temperature to substitute the respective cations into the NFO structure effectively. The latter feature is about the magnitude of *d*-spacing values. The increase in the *d*-spacing, after the substitution, is attributed to the replacement of a smaller cation (Fe^{3+}) by cations (Mg^{2+} and In^{3+}) of larger sizes, which induces the lattice distortion, leading to the expansion, i.e., *d*-spacing enhancement, compared to intrinsic NFO. The selected area electron diffraction (SAED) patterns of the calcined samples are shown in the right panel of Figure 2. In all of the SAED patterns, well-defined concentric circles could be seen, confirming that the ferrite samples are polycrystalline in nature.

X-ray Diffraction (XRD). The phase formation and purity of the sintered NFO and Mg^{2+}- and In^{3+}-substituted NFO samples were ascertained using XRD measurements and analyses. The XRD patterns of all of the samples sintered at a high temperature (1200 °C) are presented in Figure 3. The patterns and peaks indexed indicate that all of the samples crystallized in the cubic spinel structure with a space group of *Fd*3*m*, without any detectable secondary phases. Moreover, the diffraction peaks of the sintered samples are sharp and intense, indicating a high degree of crystallinity, which is also evident in TEM measurements made on calcined samples. Corroborating with TEM data, with the absence of peaks corresponding to impurity phases, the XRD data also suggest that the substituents (Mg^{2+} and In^{3+}) fully assimilated into the lattice structure of nickel ferrite. The peaks situated at the diffraction angles of 18.55, 30.36, 35.77, 37.40, 43.44, 53.89, 57.42, and 63.07° are assigned to the (111), (220), (311), (222), (400), (422), (511), and (440) crystal planes of the cubic spinel structure, respectively.[24] The lattice parameters of the samples extracted from the XRD data were found to be 8.339, 8.347, and 8.374 Å for $NiFe_2O_4$, $NiFe_{1.8}Mg_{0.2}O_4$, and $NiFe_{1.8}In_{0.2}O_4$, respectively. A similar increase in the lattice parameter has been observed and reported for In- and Mg-substituted spinel ferrite systems.[25−28] For instance, Shirsath et al.[26] studied the structural and magnetic properties of In-substituted nickel ferrite samples ($NiFe_{2-x}In_xO_4$) sintered at a higher temperature (1323 K) and reported an increase in the lattice parameter from 8.337 Å for $x = 0$ to 8.424 Å for $x = 0.3$. The current observation matches with the reports in the literature. A higher value of lattice parameter obtained for the substituted samples is primarily due to the replacement of a smaller cation (Fe^{3+}) by larger cations (Mg^{2+} and In^{3+}) as the ionic radii of substituents are larger than those of the Fe^{3+} in both fourfold (tetrahedral) and sixfold (octahedral) coordination environments.[29]

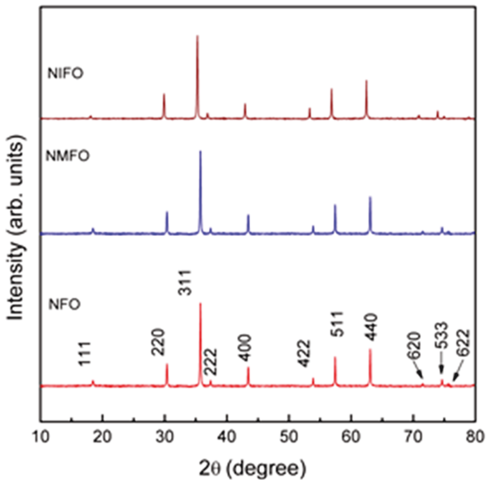

Figure 3. XRD patterns of sintered NFO, NMFO, and NIFO samples. The indexing of the diffraction peaks made according to the cubic spinel structure with a space group of *Fd*3*m* and as shown in the figure. No peaks due to impurity phases, such as Mg-oxide or In-oxide, are present, indicating the chemical quality of the ferrite compounds synthesized.

The unit cell volume was also found to increase in both NMFO and NIFO samples. The physical parameters calculated from XRD data are listed in Table 1. It can be noted (Table 1) that unlike the volume of the unit cell, the theoretical density ($\rho_{theor.}$) is lower for the NMFO compound compared to intrinsic NFO. On the other hand, the $\rho_{theor.}$ of the NIFO sample is much higher compared to that of the intrinsic NFO compound. This variation in $\rho_{theor.}$ can be interpreted reasonably on the basis of molecular mass and volume of the unit cell. The theoretical density varies proportionally with molecular mass and is inversely proportional to the volume of the unit cell using the relation

$$\rho_{theor.} = \frac{ZM}{VN_o} \tag{1}$$

where Z is the number of molecules in the unit cell (for the cubic spinel ferrite system, $Z = 8$), M is the molecular mass of the sample in gram/mole, V is the volume of the unit cell in cm^3, and N_o is the Avogadro's number ($N_o = 6.023 \times 10^{23}$ molecules/mole). In comparison with the parent compound, the molecular mass of NMFO is considerably lower but has a higher unit cell volume. Therefore, theoretical density decreases for the Mg-substituted NFO. On the other hand, both molecular mass and unit cell volume of the NIFO are significantly higher than those of the parent compound. However, the magnitude of increase in molecular mass is more pronounced than that of the unit cell volume and results in an overall increase in $\rho_{theor.}$ for In-doped NFO.

Table 1. Lattice Parameter (a), Unit Cell Volume (V), Theoretical and Experimental Densities of the Intrinsic and Mg- and In-substituted Ni Ferrite Materials

sample	a (Å) (±0.003)	V (10^{-24} cm^3) (±0.3)	$\rho_{theor.}$ (g/cm^3) (±0.03)	$\rho_{exp.}$ (g/cm^3) (±0.02)
$NiFe_2O_4$	8.339	579.8	5.37	4.62
$NiFe_{1.8}Mg_{0.2}O_4$	8.347	581.5	5.21	4.43
$NiFe_{1.8}In_{0.2}O_4$	8.374	587.2	5.56	4.84

Chemical Bonding and Elemental Analysis. *EDS Elemental Analysis.* The EDS analysis helps to identify various elements present in the sample in addition to

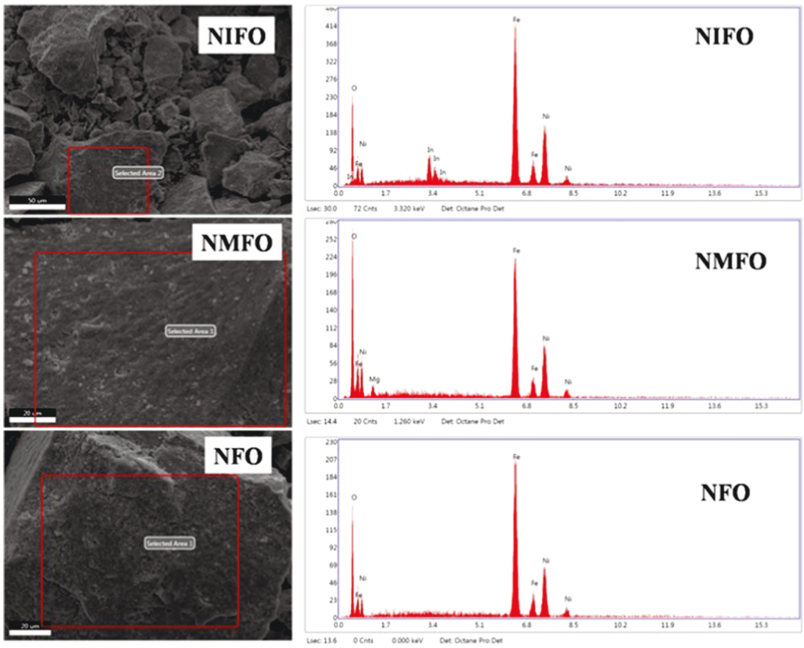

Figure 4. EDS spectra of the NFO, NMFO, and NIFO samples. The data are representative of the scans captured on the selected areas of the sample surface.

information on the chemical homogeneity.[30,31] To accurately probe the chemical information, the EDS spectra of the samples were recorded from different selected areas, and the results are shown in Figure 4. As can be seen from the images, all of the elements corresponding to the compositions of the samples are present, and no other elements were found. Note that the X-ray energy is characteristic of a specific atom involved in the X-ray generation.[30,31] Therefore, the detection of X-rays emitted provides the signature of the atoms present.[30,31] As such, EDS measurements and mapping analyses can be used to qualitatively discuss the chemical quality and chemical homogeneity of NFO, NMFO, and NIFO samples. To extract the elemental compositions of each sample, more than four EDS spectra on different spots of the samples were recorded from each sample, and the average values of weight % and atomic % were calculated. The obtained weight % (wt %) and atomic % (at %) values of all three samples are compared with the target compositions in Table 2. It is evident (Table 2) that the wt % and at % values estimated from the EDS spectra are comparable to the values of target compositions. This observation validates the fact that either the synthetic method or the processing conditions adapted for the sample preparation did not alter the composition of the intrinsic as well as Mg-/In-substituted ferrite samples. Such chemical homogeneity and uniform distribution of cations and dopants were evidenced in Mn-substituted cobalt ferrites.[32] Thus, in the present work on nickel ferrites coupled with our previous studies on cobalt ferrites, we can conclusively confirm that the chemical synthesis route as well as processing conditions employed results in the uniform and chemically homogeneous samples.

Table 2. Comparison of the Elemental Composition of the NFO, NMFO, and NIFO Samples Obtained from the EDS Analysis with that of the Target Composition

sample	elements	target elemental composition weight %	target elemental composition atomic %	elemental composition estimated from EDS analysis weight %	elemental composition estimated from EDS analysis atomic %
$NiFe_2O_4$	Ni	25	14	25	16
	Fe	48	29	54	36
$NiFe_{1.8}Mg_{0.2}O_4$	Ni	26	14	25	15
	Fe	44	26	48	30
	Mg	2	3	3	4
$NiFe_{1.8}In_{0.2}O_4$	Ni	24	14	25	15
	Fe	41	26	44	28
	In	9	3	7	2

FTIR Spectroscopy. Spectroscopic analyses provide direct information on the chemical bonding; they are quite useful, particularly to probe the dopant-induced changes (if any).[32−35] In fact, the vibrational spectroscopic analyses proved to be quite useful to understand the effect of metal-ion-substitution on the magnetic ion site in simple and complex metal oxides.[32−35] Therefore, in the present work, we relied on FTIR measurements to understand the chemical bonding and Mg/In-substitution-induced changes (if any) in the chemical bonding in nickel ferrite materials. The FTIR spectra of sintered NFO, NMFO, and NIFO samples are shown in Figure 5. It is well-known that spinel ferrite systems demonstrate two prominent fundamental absorption bands in the wavenumber region below 1000 cm^{-1} and emanate from the different metal ions located in the two crystallographic sites (tetrahedral and octahedral) of the spinel ferrites.[32,33] The absorption band situated at a lower wavenumber (~408 cm^{-1}), designated as ν_1, is contributed by the metal−oxygen (M−O) intrinsic stretching vibration in the octahedral unit (MO_6), whereas the higher wavenumber (~567 cm^{-1}), designated as ν_2, is attributed to the metal−oxygen (M−O) intrinsic stretching vibration in the tetrahedral unit (MO_4). The higher stretching frequency of the MO_4 unit is mainly due to the shorter M−O bond length as compared to that of M−O bond length of the MO_6 unit.[36,37] The frequencies of the absorption bands

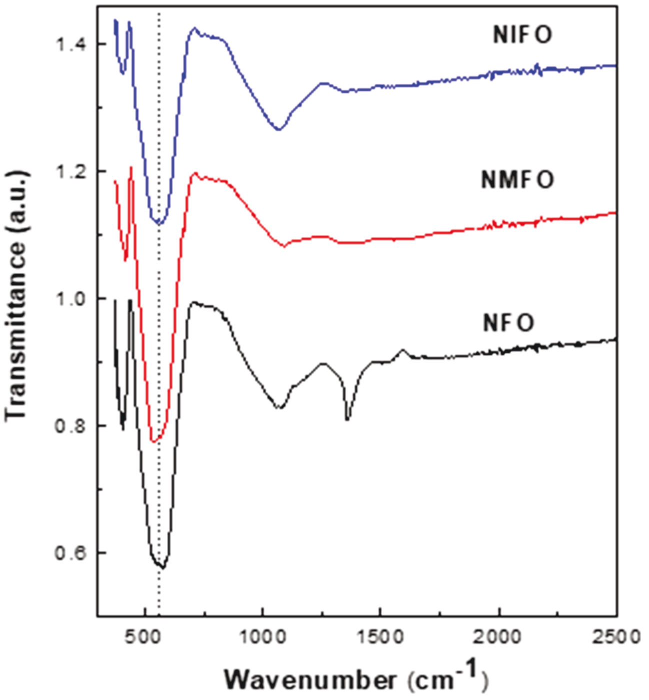

Figure 5. FTIR spectra of NFO ($NiFe_2O_4$), NMFO ($NiMg_{0.2}Fe_{1.8}O_4$), and NIFO ($NiIn_{0.2}Fe_{1.8}O_4$) samples, recorded at room temperature.

obtained for the parent compound (NFO) are in accordance with the reported values in the literature.[38] The values of the absorbance bands of all of the samples are listed in Table 3. In the case of the NMFO sample, the ν_1 and ν_2 bands shifted to a higher wavenumber (blue shift) and lower wavenumber (red shift), respectively, compared with the intrinsic nickel ferrite NFO sample. This is due to the Mg-substitution at the octahedral site. The atomic weight of Mg (24.3 amu) is nearly twofold lower than Fe atomic weight (55.8 amu), and therefore, a higher stretching frequency is necessary to stretch the Mg−O band compared to the Fe−O band at the octahedral sites. In the case of the NIFO sample, the band position of ν_1 remains the same, but that of ν_2 shifted to lower wavenumbers (red shift); this clearly suggests that In^{3+} ions have been substituted at the tetrahedral site. The observed red shift of the ν_2 band is primarily due to synergistic effects of atomic mass and longer bond length (In-O > Fe−O bond length).[25,27] In addition to the bands contributed by the spinel ferrite phase, other characteristic broad bands situated at wavenumbers ~1100 cm^{-1} have been observed for all of the samples and are attributed to the out-of-plane bending vibrations of O−H stretching of the H_2O molecules physically adsorbed over the surface of the samples.

Table 3. Infrared Absorption Bands Observed for the NFO, NMFO, and NIFO Samples

	absorption bands	
sample	ν_1 (cm^{-1})	ν_2 (cm^{-1})
NFO	408	567
NMFO	419	549
NIFO	408	561

Chemical and Cation Distribution. ^{57}Fe Mössbauer spectroscopy provides accurate information on Fe^{3+} content located in the different crystallographic sites (A- and B-sites) of the spinel-structured ferrites, such as cobalt-, nickel-, magnesium- and manganese-ferrites. The cation distribution in NFO, NMFO, and NIFO was effectively probed using Mossbauer spectra, which are shown in Figure 6. The least-squares-fitted Mossbauer spectra of all of the ferrite samples are presented in Figure 6. All of the spectra fitted using the NORMOS program and the fitting parameters, also known as hyperfine parameters, such as isomeric shift (δ), nuclear quadrupole level shift (Δ), magnetic hyperfine field (B_{hf}), and line-width (Γ) are listed in Table 4. It is evident from Figure 6 that all three samples exhibited a well-defined two-sextet pattern, primarily due to the random distribution of ferric ions (Fe^{3+}) among the tetrahedral and octahedral coordination sites of the spinel ferrite. As widely documented in the literature,[3,39,40] the sextet with a higher magnitude of magnetic hyperfine field (B_{hf}) is contributed by the tetrahedral Fe^{3+} ions, whereas the sextet with a lower magnitude of B_{hf} is due to the

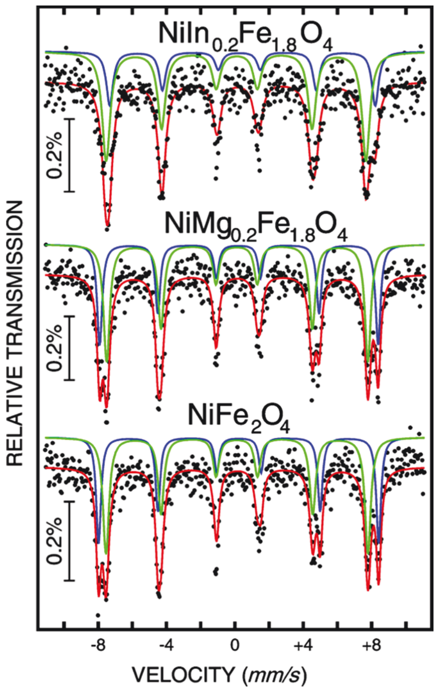

Figure 6. Mossbauer spectra of NFO, NMFO, and NIFO samples. The least-squares fitted curves are as shown in the figure. All of the spectra fitted using the NORMOS program to obtain hyperfine parameters, namely, the isomeric shift (δ), nuclear quadrupole level shift (Δ), magnetic hyperfine field (B_{hf}), and line-width (Γ). The data have been used to derive the cation distribution in NFO, NMFO, and NIFO sintered materials.

Table 4. Mossbauer Parameters for the Intrinsic and Mg- and In-substituted NFO

sample	site	δ (mm/s)	Δ (mm/s)	B_{hf} (T)	Γ (mm/s)	area (%)
$NiFe_2O_4$	A	0.23	−0.017	50.8	0.33	42
	B	0.11	0.005	47.5	0.42	58
$NiFe_{1.8}Mg_{0.2}O_4$	A	0.22	0.030	50.5	0.35	41
	B	0.12	0.035	47.4	0.43	59
$NiFe_{1.8}In_{0.2}O_4$	A	0.35	0.187	48.18	0.47	29
	B	0.09	−0.045	47.12	0.57	71

octahedral Fe^{3+} ions[3]. The area under the curve of the subspectrum reveals the percent of iron content in the respective crystallographic sites. For the unsubstituted nickel ferrite sample, the percentages of area are found to be 42 and 58%, respectively, for A-site and B-site sublattices and the corresponding cation distribution is obtained as $[Ni_{0.16}Fe_{0.84}]_A[Ni_{0.84}Fe_{1.16}]_B$. This distribution is nearly comparable to the reported cation distribution for the Ni-ferrite.[41]

Compared with intrinsic NFO, no significant changes in the area, line-width, and the magnetic hyperfine field are observed for NMFO. However, in the case of In-substituted NFO, an area corresponding to the A-site is considerably lower than that observed for the intrinsic nickel ferrite sample. This is mainly due to the replacement of an equivalent amount of Fe^{3+} by nonmagnetic In^{3+} ions at the tetrahedral sites. Also, the line width of the A- and B-sublattices of $NiFe_{1.8}In_{0.2}O_4$ is considerably higher than that of the other two samples due to the presence of In^{3+} at the tetrahedral sites that changes the magnetic interaction between A- and B-sites cations. As each A-site cation is surrounded by 12 B-site cations and each B-site cation is coupled magnetically with only six A-site cations,[42] the substitution of the nonmagnetic cation In^{3+} at the tetrahedral sites significantly reduces the magnetic interaction between A-sites and B-sites and hence the lower B_{hf} value for the A-site of NIFO. A similar feature has been reported for In-substituted spinel ferrite systems.[25,43] The cation distributions of the NFO, NMFO, and NIFO samples are listed in Table 5.

Table 5. Cations Distribution in the Tetrahedral (A-site) and Octahedral (B-site) Sites of the Spinel Ferrite[a]

sample	A-site	B-site
$NiFe_2O_4$	$Ni_{0.16}Fe_{0.84}$	$Ni_{0.84}Fe_{1.16}$
$NiMg_{0.2}Fe_{1.8}O_4$	$Ni_{0.26}Fe_{0.74}$	$Mg_{0.2}Ni_{0.74}Fe_{1.06}$
$NiIn_{0.2}Fe_{1.8}O_4$	$In_{0.2}Ni_{0.28}Fe_{0.52}$	$Ni_{0.72}Fe_{1.28}$

[a] The cation distribution in intrinsic as well as Mg- and In-substituted NFO included.

Electronic Structure and Chemical Valence State Analysis. X-ray photoelectron spectroscopy (XPS) is a very valuable analytical technique to investigate the electronic structure, chemical valence states, and qualitative analysis of various elements present in the samples.[44,45] In addition, it is possible to determine the cation distribution of the spinel ferrites through the deconvolution of the resultant XPS spectra of the sample.[46] In the present study, XPS spectra of NFO, NMFO, and NIFO samples were recorded using carbon as an internal reference material, and the resultant survey spectra are shown in Figure 7. It is evident from the survey spectra that all of the elements corresponding to the respective sample composition are present. The results and observations of XPS characteristic peaks with respect to various elements are in good agreement with the results of the EDS analysis. To extract further detailed information on individual elements (Fe, Ni, In, Mg) of the samples, high-resolution spectra of the elements were deconvoluted, using the standard procedures,[44,45] after correction using carbon 1s peak (284.6 eV).

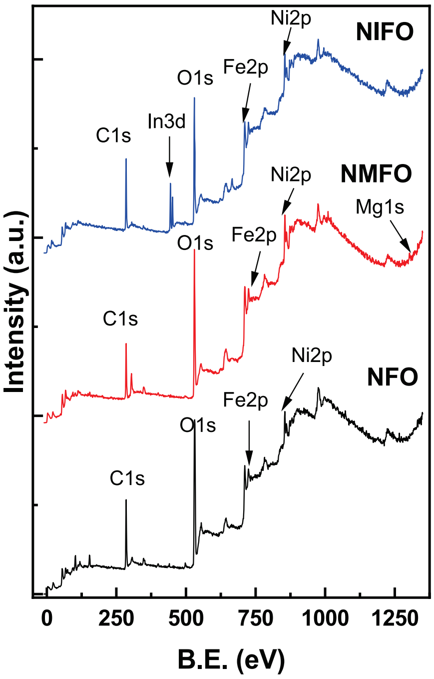

Figure 7. XPS survey spectra of NFO, NMFO, and NIFO samples. The respective XPS peaks identified and corresponding binding energy positions are as indicated.

The detailed core-level peaks, i.e., the deconvoluted XPS spectra, of Fe, Ni, In, and Mg are presented in Figure 8. In the XPS spectra of Fe (Figure 8a), two major peaks situated at binding energy (BE) values of ∼710 and ∼724 eV are observed. These two correspond to the spin−orbit doublet of Fe 2p, i.e., Fe $2p_{3/2}$ and Fe $2p_{1/2}$, respectively.[46] The broad and intense Fe $2p_{3/2}$ peak has been deconvoluted into two subpeaks, pertaining to ferric ions (Fe^{3+}) in two different crystallographic environments (tetrahedral and octahedral sites). The BE and area under the curves of Fe^{3+} in the B- and A-sites are tabulated in Table 6. It can be noted that the XPS data of the Fe 2p core-level indicates the characteristic of Fe ions predominantly in the Fe^{3+} state. Furthermore, the BE values are comparable to those reported in the literature values.[46,47] It is worth mentioning here that both $2p_{3/2}$ and $2p_{1/2}$ peaks are accompanied by low-intensity satellite peaks at ∼718.8 and ∼734 eV, signifying that all of the samples predominantly comprised Fe^{3+}.

Similar to XPS spectra of Fe, two major XPS peaks have been observed for Ni (Figure 8b) at BE values ∼856.5 eV and ∼875.5 eV and are assigned to Ni $2p_{3/2}$ and Ni $p_{1/2}$, respectively. Here again, the main Ni $2p_{3/2}$ peaks in all of the samples were deconvoluted, and the corresponding BE values are listed in Table 6. These values are comparable to the reported BEs of Ni^{2+} in nickel ferrite.[47] Unlike the XPS spectra of Fe, the intensities of the satellite peaks of Ni $2p_{3/2}$ and Ni $2p_{1/2}$ are significantly higher due to the fact that all samples consist of a higher concentration of Ni^{2+} ions.[47] An attempt has been made to estimate the cation distribution of the samples using the areas under the curves of the cations (Fe and Ni). The results are presented in Table 7. It is important to note that for all of the samples, the cation distribution obtained from the XPS analysis is comparable to that obtained from the Mossbauer analysis. The marginal discrepancies of the cation distribution found from two different techniques can be attributed to the error while taking the baseline and deconvolution the spectra, i.e., postprocessing analysis of the XPS spectral data.

Two prominent peaks situated at binding energies of 443.96 and 451.51 eV are observed in the XPS spectrum of indium (see Figure 8c) and are designated as In $3d_{5/2}$ and In $3d_{3/2}$,

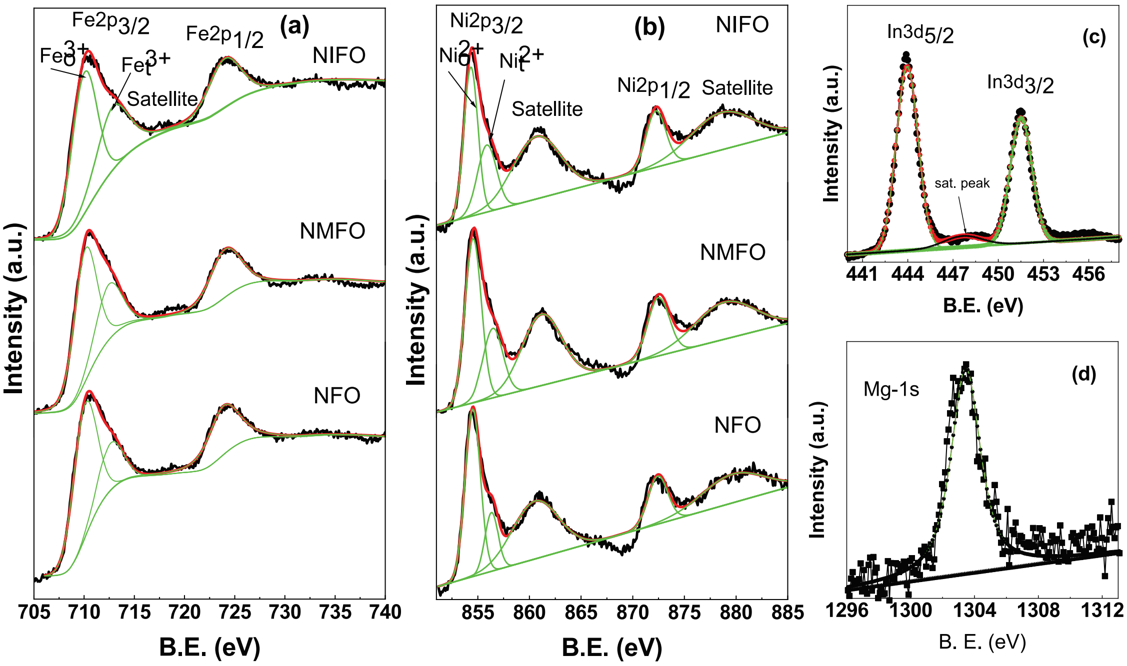

Figure 8. High-resolution XPS spectra of (a) Fe 2p, (b) Ni 2p, (c) In 3d, and (d) Mg 1s. The data shown are for NFO, NMFO, and NIFO samples.

Table 6. Binding Energies (BE) of Fe^{3+} and Ni^{2+} Located at the A- and B-sites and the Relative Areas under the Curves of $2p_{3/2}$ Main and Its Satellite Peaks for the Sintered NFO, NMFO, and NIFO Samples

	Fe					Ni						
	Fe $2p_{3/2}$					Ni $2p_{3/2}$					Ni $2p_{1/2}$	
sample	B-site B.E. (eV)	B-site area	A-site B.E. (eV)	A-site area	Fe $2p_{1/2}$ B.E. (eV)	B-site B.E. (eV)	B-site area	A-site B.E. (eV)	A-site area	Sat. B.E.	B.E. (eV)	Sat. B.E.
NFO	710.1	1600	712.6	900	723.9	854.4	1584	856.2	616	860.6	872.4	879.6
NMFO	710.1	1543	712.4	980	724.0	854.5	1534	856.4	689	861.1	872.5	878.9
NIFO	710.0	1675	712.8	848	723.9	854.3	1798	855.8	422	860.7	872.2	878.6

Table 7. Cation Distribution in the Tetrahedral (A-site) and Octahedral (B-site) Sites of the Spinel Ferrite Samples, Obtained from the XPS Analysis

sample	A-site	B-site
$NiFe_2O_4$	$Ni_{0.28}Fe_{0.72}$	$Ni_{0.72}Fe_{1.28}$
$NiMg_{0.2}Fe_{1.8}O_4$	$Ni_{0.26}Fe_{0.69}$	$Mg_{0.2}Ni_{0.69}Fe_{1.11}$
$NiIn_{0.2}Fe_{1.8}O_4$	$In_{0.2}Ni_{0.19}Fe_{0.61}$	$Ni_{0.81}Fe_{1.19}$

respectively. These peak positions are in good agreement with those reported in the literature.[48] Both In $3d_{5/2}$ and In $3d_{3/2}$ peaks are accompanied by low-intensity satellite peaks centered at 447.65 and 455.46 eV. A single and nearly symmetric peak centered at 1303.4 eV can be seen in the 1s spectrum of magnesium (Figure 8d). The symmetrical nature of the 1S peak of Mg signifies that Mg^{2+} occupies a specific crystallographic site, preferably octahedral sites of the spinel ferrite.[49]

Finally, Figure 9 shows the O 1s core-level XPS spectra of all three samples. In the spectrum of the unsubstituted NFO sample, two peaks with almost equal intensities are observed at binding energies of 529.58 and 531.58 eV and are attributed to lattice oxygen and chemically adsorbed oxygen on the surface.[49] However, in the case of substituted samples (NIFO and NMFO), the intensity of the 531.58 eV peak is significantly lower than that of the NFO sample, probably due

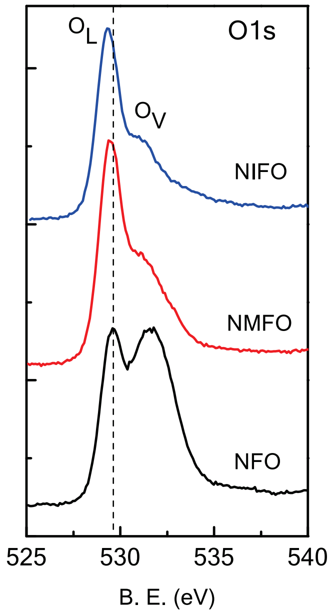

Figure 9. Oxygen 1s core-level XPS data of NFO, NMFO, and NIFO samples.

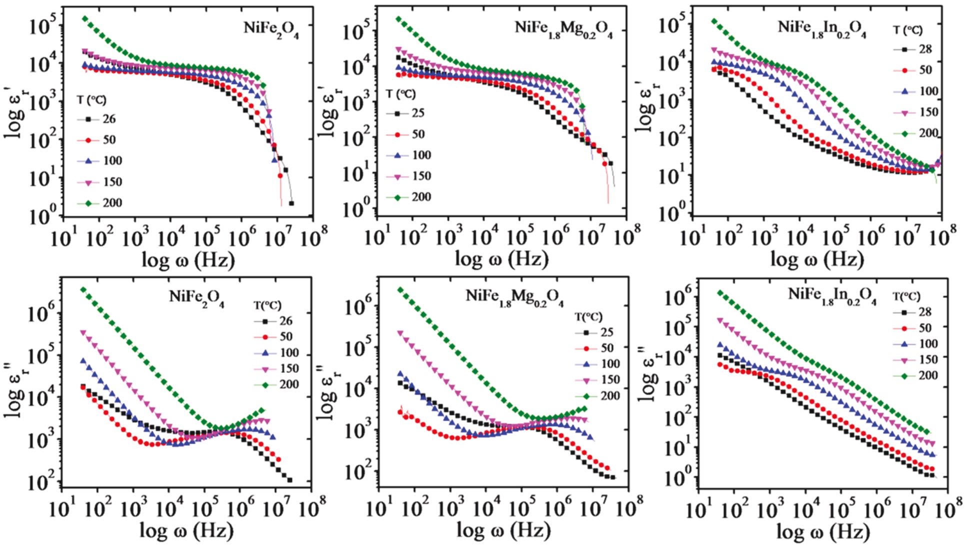

Figure 10. Real and imaginary parts of the dielectric constant for $NiFe_2O_4$, $NiFe_{1.8}Mg_{0.2}O_4$, and $NiFe_{1.8}In_{0.2}O_4$ obtained at varying temperatures in the range of 25−200 °C.

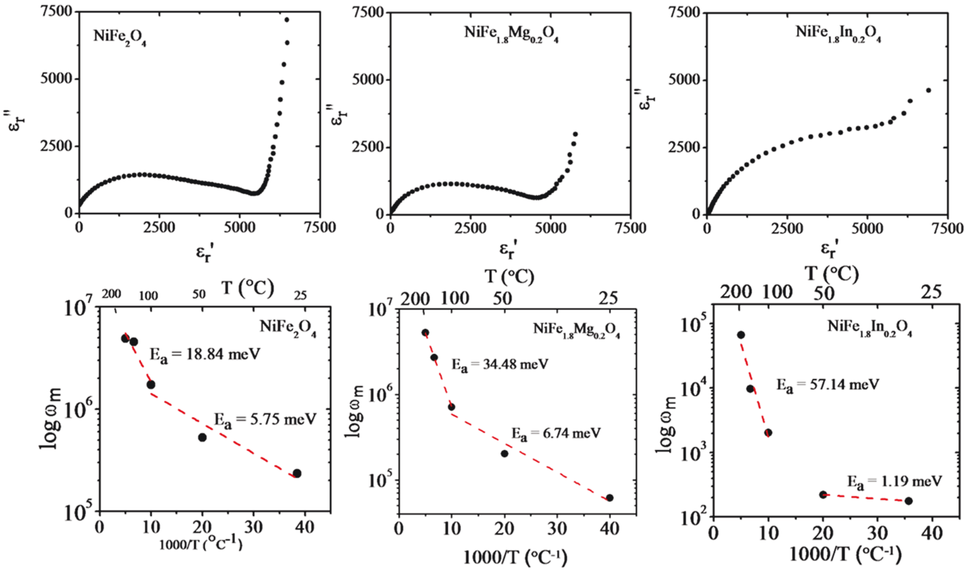

Figure 11. Cole−Cole plots (top panel) for $NiFe_2O_4$, $NiFe_{1.8}Mg_{0.2}O_4$, and $NiFe_{1.8}In_{0.2}O_4$ samples at 50 °C. The activation energy determination for the respective samples is also shown (bottom panel).

to less adsorbed oxygen over the surface of the samples. Also, the position of the 529.58 eV peak of the NIFO and NMFO samples shifted to lower binding energies owing to the effect of metal-ion doping.

Dielectric Properties. Figure 10 shows real (ε_r') and imaginary (ε_r'') parts of the dielectric constant of $NiFe_2O_4$, $NiFe_{1.8}Mg_{0.2}O_4$, and $NiFe_{1.8}In_{0.2}O_4$ samples. The temperature (25−200 °C)-dependent dielectric data measured in the frequency range of 40 Hz−100 MHz are shown. For $NiFe_2O_4$, the real part of the dielectric constant seems very high (∼6000) at a lower frequency (40 Hz) and remains nearly constant with increasing frequency. However, at or above 10 kHz, this value starts decreasing while revealing a steplike feature at a higher frequency. Consequently, the imaginary part of the dielectric constant shows a relaxation peak at 0.5 MHz. The high value of the dielectric constant at a lower frequency (40 Hz) is due to Maxwell−Wagner (M−W)-type interfacial polarization effect.[50,51] This occurs due to free charge carriers present in the materials. With increasing frequency, these free charge carriers do not follow field change, and hence space charge polarization decreases with increasing frequency, leaving only dipolar polarization; this explains the constant value of the real part of the dielectric constant till 10 kHz frequency. Above this frequency, dipolar contribution toward the dielectric constant starts decreasing, leaving behind the steplike feature in the real part and the dielectric loss peak in the imaginary part of the dielectric constant. In conclusion, the frequency-dependent dielectric constant dispersion of $NiFe_2O_4$ shows a high value of dielectric constant at a lower frequency due to the M−W type and dipolar polarization, which is sustained and finally suppressed with further frequency.

It is also observed that with an increase in temperature, ε_r' plots indicate an increase in the dielectric constant (at lower frequency) while shifting the dipolar relaxation at a higher frequency end. The increase in the dielectric constant at a lower frequency is due to the increase in the number of free charge carriers with temperature.[52] As the temperature increases, more number of free charge carriers contribute to the interfacial polarization. The shifting of dipolar polarization at a higher frequency is due to the decrease in the relaxation time for dipolar polarization. The origin of dipolar polarization in the ferrites system is due to the response of the cations (Mg^{2+}, Fe^{3+}, and In^{3+}) with respect to the oxygen octahedra and tetrahedron. With increasing temperature, dipoles respond by means of thermally activated dipole interactions, which explains the shifting of relaxation of dipolar polarization at a higher frequency end. Similar behavior was also observed in $NiFe_{1.8}Mg_{0.2}O_4$ and $NiFe_{1.8}In_{0.2}O_4$ samples, as shown in Figure 10, with respect to an increase in the frequency and temperature. It is interesting to see the dipolar polarization of the $NiFe_{1.8}In_{0.2}O_4$ sample, whose dipolar relaxation starts very early at 200 Hz as compared to the other two samples. This is due to In^{3+} having larger ionic radii as compared to Mg^{2+} and Fe^{3+}.

Figure 11 shows the cole−cole plots for the dipolar relaxation for $NiFe_2O_4$, $NiFe_{1.8}Mg_{0.2}O_4$, and $NiFe_{1.8}In_{0.2}O_4$ samples at 50 °C. From the plots, it is observed that there exists a straight line followed by a distorted semicircle with an increase in frequency. This tail-like straight line is due to the free charge carriers as explained above, and the semicircular curve is due to the dipolar polarization. It is observed that there are two depressed semicircles (prominent for $NiFe_2O_4$ and $NiFe_{1.8}Mg_{0.2}O_4$) whose center lies below the real axis. This indicates the presence of dipolar polarization due to the two different types of charge species. One is due to the response of the cations at the tetrahedral site, and another is due to the response at the octahedral site. For NIFO, a single semicircle was observed, which is due to the enhanced effect of the tetrahedral site. In the In-substituted sample (NIFO), In^{3+}occupies the tetrahedral site. Activation energy calculated for NFO, NFMO, and NIFO samples are as follows: 18.84, 5.75; 34.48, 6.74; and 57.14, 1.19 meV, respectively. The high value of NIFO could be due to the enhanced dipolar effect of In^{3+} located at the tetrahedral site.

■ SUMMARY AND CONCLUSIONS

We demonstrated the tunable dielectric properties derived in Mg- and In-substituted nickel ferrite, where the selective crystallographic site occupation of the dopant cation is evident. High-quality NFO, NMFO, and NIFO materials were realized by a simple tartrate-gel chemical route. Structural studies indicate the formation of defect-free, single-phase spinel-structured NFO, NMFO, and NIFO nanomaterials. The Mg^{2+} occupies the octahedral site, while In^{3+} occupies the tetrahedral site of the spinel-structured NFO. The cation distribution obtained from Mossbauer studies accounts for the dielectric properties of all of the samples as a function of variable temperature. The electronic structure and chemical valence state analysis using XPS corroborate with chemical bonding analyses made using FTIR and cation distribution by Mossbauer spectroscopy. Overall, the FTIR and XPS along with EDS analyses validate the chemical homogeneity of the NFO, NFMO, and NIFO samples. The differences and tunable dielectric properties obtained in these materials are primarily due to the size effect and site preference of dopants (Mg^{2+} and In^{3+}). A thermally activated electrical conduction mechanism was operative in NFO, NMFO, and NIFO materials. Due to the enhanced dipolar effect of In^{3+} at the tetrahedral site compared to Mg^{2+} at the octahedral site, the activation energy of NIFO is relatively higher compared to intrinsic and Mg-substituted NFO materials.

■ AUTHOR INFORMATION

Corresponding Authors

Pendaranahalli Nadikeraiah Anantharamaiah − *Department of Chemistry, Faculty of Mathematical and Physical Sciences, M. S. Ramaiah University of Applied Sciences, Bangalore 560058, India;* orcid.org/0000-0001-8919-3686; Email: anantha.chem@gmail.com

C. V. Ramana − *Center for Advanced Materials Research (CMR), University of Texas at El Paso, El Paso, Texas 79968, United States; Department of Mechanical Engineering, University of Texas at El Paso, El Paso, Texas 79968, United States;* orcid.org/0000-0002-5286-3065; Email: rvchintalapalle@utep.edu

Authors

Prerna Rao − *Department of Physics, Faculty of Mathematical and Physical Sciences, M. S. Ramaiah University of Applied Sciences, Bangalore 560058, India*

Hadonahalli Munegowda Shashanka − *Department of Chemistry, Faculty of Mathematical and Physical Sciences, M. S. Ramaiah University of Applied Sciences, Bangalore 560058, India*

Vijay Khopkar − *Materials Research Centre, Indian Institute of Science, Bangalore 560012, India*

Jeyaramane Arout Chelvane − *Advanced Magnetic Group, Defence Metallurgical Research Laboratory (DMRL), Hyderabad 500058, India*

Balaram Sahoo − *Materials Research Centre, Indian Institute of Science, Bangalore 560012, India;* orcid.org/0000-0002-2050-4746

Complete contact information is available at: https://pubs.acs.org/10.1021/acs.jpcc.2c00529

Notes

The authors declare no competing financial interest.

■ ACKNOWLEDGMENTS

C.V.R. acknowledges, with pleasure, support from the National Science Foundation (NSF) with NSF-PREM grant #DMR-1827745.

■ REFERENCES

(1) George, M.; John, A. M.; Nair, S. S.; Joy, P. A.; Anantharaman, M. R. Finite Size Effects on the Structural and Magnetic Properties of Sol−Gel Synthesized $NiFe_2O_4$ Powders. *J. Magn. Magn. Mater.* **2006**, *302*, 190−195.

(2) Peng, E.; Wei, X.; Herng, T. S.; Garbe, U.; Yub, D.; Jun Ding, J. Ferrite-Based Soft and Hard Magnetic Structures by Extrusion Free-Forming. *RSC Adv.* **2017**, *7*, 27128.

(3) Amini, M.; Kamkar, M.; Rahmani, F.; Ghaffarkhah, A.; Ahmadijokani, F.; Arjmand, M. Multilayer Structures of a $Zn_{0.5}Ni_{0.5}Fe_2O_4$-Reduced Graphene Oxide/PVDF Nanocomposite for Tunable and Highly Efficient Microwave Absorbers. *ACS Appl. Electron. Mater.* **2021**, *3*, 5514−5527.

(4) Wang, Y.; Qi, Q.; Guang Yin, G.; Wang, W.; Yu, D. Flexible, Ultralight, and Mechanically Robust Waterborne Polyurethane/$Ti_3C_2T_x$ MXene/Nickel Ferrite Hybrid Aerogels for High-Performance Electromagnetic Interference Shielding. *ACS Appl. Mater. Interfaces* **2021**, *13*, 21831−21843.

(5) Wang, Y.; Li, L.; Zhang, Y.; Chen, X.; Fang, S.; Li, G. Growth Kinetics, Cation Occupancy, and Magnetic Properties of Multimetal

Oxide Nanoparticles: A Case Study on Spinel $NiFe_2O_4$. *J. Phys. Chem. C* **2017**, *121*, 19467−19477.

(6) Alijani, H. Q.; Iravani, S.; Pourseyedi, S.; Torkzadeh-Mahani, M.; Barani, M.; Khatami, M. Biosynthesis of spinel nickel ferrite nanowhiskers and their biomedical applications. *Sci. Rep.* **2021**, *11*, No. 17431.

(7) Anantharamaiah, P. N.; Mondal, S.; Manasa, K. S.; Saha, S.; Pai, M. Enhancing the catalytic activity of recyclable nanocrystalline $NiFe_2O_4$ by replacing Ni by Cu. *Ceram. Int.* **2020**, *46*, 1220−1226.

(8) Kakade, S. G.; Ma, Y.-R.; Devan, R. S.; Kolekar, Y. D.; Ramana, C. V. Dielectric, Complex Impedance, and Electrical Transport Properties of Erbium (Er^{3+}) Ion-Substituted Nanocrystalline, Cobalt-Rich Ferrite ($Co_{1.1}Fe_{1.9-x}Er_xO_4$). *J. Phys. Chem. C* **2016**, *120*, 5682−5693.

(9) Shirsath, S. E.; Wang, D.; Zhang, J.; Morisako, A.; Li, S.; Liu, X. Single-Crystal-like Textured Growth of $CoFe_2O_4$ Thin Film on an Amorphous Substrate: A Self-Bilayer Approach. *ACS Appl. Electron. Mater.* **2020**, *2*, 3650−3657.

(10) Choi, M.; Shim, S-J.; Jung, Y.; Kim, H-S.; Seo, B.-K. The Effect of Annealing Temperature on the Synthesis of Nickel Ferrite Films as High-Capacity Anode Materials for Lithium Ion Batteries. *Nanomaterials* **2021**, *11*, 3238.

(11) Narang, S. B.; Pubby, K. Nickel Spinel Ferrites: A Review. *J. Magn. Magn. Mater.* **2021**, *519*, No. 167163.

(12) Bharathi, K. K.; Markandeyulu, G.; Ramana, C. V. Structural, Magnetic, Electrical, And Magnetoelectric Properties of Sm- and Ho-Substituted Nickel Ferrites. *J. Phys. Chem. C* **2011**, *115*, 554−560.

(13) Hao, A.; Ismail, M.; He, S.; Qin, N.; Huang, W.; Wu, J.; Bao, D. Improved Unipolar Resistive Switching Characteristics of Au-doped Nickel Ferrite Magnetic Thin Films for Nonvolatile Memory Applications. *J. Alloys Compd.* **2018**, *732*, 573−584.

(14) Liu, F.; Liu, J.; Fang, R.; Li, Y.; Yang, Y. Different Reactivities of the (100) and (110) Surfaces of the $NiFe_2O_4$ Composite Oxygen Carrier in Chemical Looping Combustion: An Atomic Insight. *J. Phys. Chem. C* **2021**, *125*, 19190−19199.

(15) Kamala Bharathi, K.; Chelvane, J. A.; Markandeyulu, G. Magnetoelectric Properties of Gd and Nd-doped Nickel Ferrite. *J. Magn. Magn. Mater.* **2009**, *321*, 3677−3680.

(16) Patange, S. M.; Shirsath, S. E.; Toksha, B. G.; Jadhav, S. S.; Jadhav, K. M. Electrical and Magnetic Properties of Cr^{3+} Substituted Nanocrystalline Nickel Ferrite. *J. Appl. Phys.* **2009**, *106*, No. 023914.

(17) Manikandan, V.; Mirzaei, A.; Vigneselvan, S.; Kavita, S.; Mane, R. S.; Kim, S. S.; Chandrasekaran, J. Role of Ruthenium in the Dielectric, Magnetic Properties of Nickel Ferrite (Ru−$NiFe_2O_4$) Nanoparticles and Their Application in Hydrogen Sensors. *ACS Omega* **2019**, *4*, 12919−12926.

(18) O'Brien, C. J.; Rák, Zs.; Brenner, D. W. Calculated Stability and Structure of Nickel Ferrite Crystal Surfaces in Hydrothermal Environments. *J. Phys. Chem. C* **2014**, *118*, 5414−5423.

(19) Ishaque, M.; Islam, M. U.; Khan, M. A.; Rahman, I. Z.; Genson, A.; Hampshire, S. Structural, Electrical and Dielectric Properties of Yttrium Substituted Nickel Ferrites. *Phys. B* **2010**, *405*, 1532−1540.

(20) Ghosh, M. P.; Kumar, P.; Kar, M.; Mukherjee, S. Impact of In^{3+}Ion Substitution on Microstructural, Magnetic and Dielectric Responses of Nickel−Cobalt Spinel Ferrite Nanocrystals. *J. Mater. Sci.: Mater. Electron.* **2020**, *31*, 17762−17772.

(21) Heiba, Z. K.; Mohamed, M. B.; Ahmed, M. A.; Moussa, M. A. A.; Hamdeh, H. H. Cation Distribution and Dielectric Properties of Nanocrystalline Gallium Substituted Nickel Ferrite. *J. Alloys Compd.* **2014**, *586*, 773−781.

(22) Sonia, M. M. L.; Anand, S.; Vinosel, V. M.; Jenifer, M. A.; Pauline, S. Effect of Lattice Strain on Structural, Magnetic and Dielectric Properties of Sol−Gel Synthesized Nanocrystalline Ce^{3+} Substituted Nickel Ferrite. *J. Mater. Sci.: Mater. Electron.* **2018**, *29*, 15006−15021.

(23) Moradmard, H.; Shayesteh, S. F.; Tohidi, P.; Abbas, Z.; Khaleghi, M. Structural, Magnetic and Dielectric Properties of Magnesium Doped Nickel Ferrite Nanoparticles. *J. Alloys Compd.* **2015**, *650*, 116−122.

(24) Anantharamaiah, P. N.; Rao, B. P.; Shashanka, H. M.; Chelvane, J. A.; Khopkar, V.; Sahoo, B. Role of Mg^{2+} and In^{3+}Substitution On Magnetic, Magnetostrictive and Dielectric Properties of $NiFe_2O_4$ Ceramics Derived from Nanopowders. *Phys. Chem. Chem. Phys.* **2021**, *23*, 1694−1705.

(25) Sumalatha, M.; Reddy, S. S. K.; Reddy, M. S.; Sripada, S.; Raja, M. M.; Reddy, C. G.; Reddy, P. Y.; Reddy, V. R. Raman and in-field ^{57}Fe Mossbauer study of cation distribution in indium (In) substituted phase pure cobalt ferrite ($CoFe_{2-x}In_xO_4$). *J. Magn. Magn. Mater.* **2021**, *521*, No. 167561.

(26) Shirsath, S. E.; Toksha, B. G.; Jadhav, K. M. Structural and magnetic properties of In^{3+} substituted $NiFe_2O_4$. *Mater. Chem. Phys.* **2009**, *117*, 163−168.

(27) Anantharamaiah, P. N.; Joy, P. A. Effect of size and site preference of trivalent non-magnetic metal ions (Al^{3+}, Ga^{3+}, In^{3+}) substituted for Fe^{3+} on the magnetostrictive properties of sintered $CoFe_2O_4$. *J. Phys. D: Appl. Phys.* **2017**, *50*, No. 435005.

(28) Chavan, P.; Naik, L. R. Investigation of energy band gap and conduction mechanism of magnesium substituted nickel ferrite nanoparticles. *Phys. Status Solidi A* **2017**, *214*, No. 1700077.

(29) Shannon, R. D. Revised Effective Ionic Radii and Systematic Studies of Interatomic Distances in Halides and Chalcogenides. *Acta Crystallogr., Sect. A: Cryst. Phys., Diffr., Theor. Gen. Crystallogr.* **1976**, *32*, 751−767.

(30) Ramana, C. V.; Ait-Salah, A.; Utsunomiya, S.; Morhange, J. F.; Mauger, A.; Gendron, F.; Julien, C. M. Spectroscopic and chemical imaging analysis of lithium iron triphosphate. *J. Phys. Chem. C* **2007**, *111*, 1049−1054.

(31) Ramana, C. V.; Ait-Salah, A.; Utsunomiya, S.; Mauger, A.; Gendron, F.; Julien, C. M. Novel lithium iron pyrophosphate ($LiFe_{1.5}P_2O_7$) as a positive electrode for Li-ion batteries. *Chem. Mater.* **2007**, *19*, 5319−5324.

(32) Ansari, S. M.; Ghosh, K. C.; Devan, R. S.; Sen, D.; Sastry, P. U.; Kolekar, Y. D.; Ramana, C. V. Eco-Friendly Synthesis, Crystal Chemistry, and Magnetic Properties of Manganese-Substituted $CoFe_2O_4$ Nanoparticles. *ACS Omega* **2020**, *5*, 19315−19330.

(33) Puli, V. S.; Adireddy, S.; Ramana, C. V. Chemical bonding and magnetic properties of gadolinium (Gd) substituted cobalt ferrite. *J. Alloys Compd.* **2015**, *644*, 470−475.

(34) Ramana, C. V.; Hussain, O. M.; Pinto, R.; Julien, C. M. Microstructural features of pulsed-laser deposited V_2O_5 thin films. *Appl. Surf. Sci.* **2003**, *207*, 135−138.

(35) Hussain, O. M.; Srinivasa Rao, K.; Madhuri, K. V.; Ramana, C. V.; Naidu, B. S.; Pai, S.; John, J.; Pinto, R.; Julien, C. M. Growth and characteristics of reactive pulsed laser deposited molybdenum trioxide thin films. *Appl. Phys. A* **2002**, *75*, 417−422.

(36) Anantharamaiah, P. N.; Giri, S. Enhancement of SO_2 Gas Sensing Performance of Co_3O_4 Spinel by Cu Substitution. *Sens. Lett.* **2020**, *18*, 83−88.

(37) Anantharamaiah, P. N.; Chandra, N. S.; Shashanka, H. M.; R Kumar, R.; Sahoo, B. Magnetic and catalytic properties of Cu-substituted $SrFe_{12}O_{19}$ synthesized by tartrate-gel method. *Adv. Powder Technol.* **2020**, *31*, 2385−2393.

(38) Parishani, M.; Nadafan, M.; Dehghani, Z.; Malekfar, R.; Khorrami, G. H. H. Optical and dielectric properties of $NiFe_2O_4$ nanoparticles under different synthesized temperature. *Results Phys.* **2017**, *7*, 3619−3623.

(39) Singhal, S.; Barthwal, S. K.; Chandra, K. XRD, Magnetic and Mössbauer Spectral Studies of Nano Size Aluminium Substituted Cobalt Ferrites ($CoAl_xFe_{2-x}O_4$). *J. Magn. Magn. Mater.* **2006**, *306*, 233−240.

(40) Kamali, S. Spin Structure, Magnetism, and Cation Distributions of $NiFe_{2-x}Al_xO_4$ Solid Solutions. *J. Magn. Magn. Mater.* **2017**, *433*, 155−161.

(41) Kumar, R. V.; Anupama, A. V.; Kumar, R.; Choudhary, H. K.; Khopkar, V. B.; Aravind, G.; Sahoo, B. Cation distributions and magnetism of Al-substituted $CoFe_2O_4$ - $NiFe_2O_4$ solid solutions synthesized by sol-gel auto-combustion method. *Ceram. Int.* **2018**, *44*, 20708−20715.

(42) Krieble, K.; Devlin, M.; Lee, S. J.; Aldini, S. T.; Snyder, J. E. Investigation of Ga Substitution in Cobalt Ferrite ($CoGa_xFe_{2-x}O_4$) using Mossbauer Spectroscopy. *J. Appl. Phys.* **2008**, *103*, No. 07E508.

(43) Hashim, M.; Raghasudha, M.; Shah, J.; Shirsath, S.; Ravinder, D.; Kumar, S.; Meena, S. S.; Bhatt, P.; Alimuddin; Kumar, R.; et al. High temperature dielectric studies of indium-substituted NiCuZn nanoferrites. *J. Phys. Chem. Solids* **2018**, *112*, 29−36.

(44) Zade, V.; Mallesham, B.; Roy, S.; Shutthanandan, V.; Ramana, C. V. Electronic Structure of Tungsten-Doped β-Ga_2O_3 Compounds. *ECS J. Solid State Sci. Technol.* **2019**, *8*, Q3111−Q3115.

(45) Ramana, C. V.; Roy, S.; Zade, V.; Battu, A. K.; Makeswaran, N.; Shutthanandan, V. Electronic Structure and chemical bonding in transition-metal-mixed gallium oxide (Ga_2O_3) compounds. *J. Phys. Chem. Solids* **2021**, *157*, No. 110174.

(46) Anantharamaiah, P. N.; Joy, P. A. Enhancing the strain sensitivity of $CoFe_2O_4$ at low magnetic fields without affecting the magnetostriction coefficient by substitution of small amounts of Mg for Fe. *Phys. Chem. Chem. Phys.* **2016**, *18*, 10516−10527.

(47) Ortiz-Quiñonez, J.-L.; Pal, U.; Villanueva, M. S. Structural, Magnetic, and Catalytic Evaluation of Spinel Co, Ni, and Co−Ni Ferrite Nanoparticles Fabricated by Low-Temperature Solution Combustion Process. *ACS Omega* **2018**, *3*, 14986−15001.

(48) Selvakumar, D.; Dharmaraj, N.; Kumar, N. S.; Padaki, V. C. Oxygen Sensing Properties of Platinum Doped Indium Oxide Nanoparticles Prepared by Hydrothermal Method. *Synth. React. Inorg., Met.-Org., Nano-Met. Chem.* **2015**, *45*, 753−758.

(49) Anantharamaiah, P. N.; KS Manasa, K. S.; YC Sunil Kumar, Y. C. S. Fabrication of magnetically recoverable and reusable $MgFe_2O_4$/Ag_3PO_4 composite for catalytic reduction of 4-Nitrophenol. *Solid State Sci.* **2020**, *106*, No. 106302.

(50) Patange, S. M.; Shirsath, S. E.; Lohar, K. S.; Jadhav, S. S.; Kulkarni, N.; Jadhav, K. M. Electrical and Switching Properties of $NiAl_xFe_{2-x}O_4$ Ferrites Synthesized by Chemical Method. *Phys. B* **2011**, *406*, 663−668.

(51) Chavan, P.; Naik, L. R.; Belavi, P. B.; Chavan, G.; Ramesha, C. K.; Kotnala, R. K. Studies on Electrical and Magnetic Properties of Mg-Substituted Nickel Ferrites. *J. Electron. Mater.* **2017**, *46*, 188−198.

(52) Hajlaoui, M. E.; Radhia Dhahri, R.; Hnainia, N.; Aida Benchaabane, A.; Essebti Dhahri, E.; Khirouni, K. Conductivity and Giant Permittivity Study of $Zn_{0.5}Ni_{0.5}Fe_2O_4$Spinel Ferrite as a Function of Frequency and Temperature. *RSC Adv.* **2019**, *9*, 32395−32402.

https://doi.org/10.1021/acs.jpcc.2c00529
J. Phys. Chem. C 2022, 126, 9123−9134